

Universal Scale-Free Non-Hermitian Skin Effect Near Bloch Point

Wei Li (李维),¹ Zhoujian Sun,¹ Ze Yang,¹ and Fuxiang Li^{1,*}

¹*School of Physics and Electronics, Hunan University, Changsha 410082, China*

(Dated: November 27, 2023)

The scale-free non-Hermitian skin effect (NHSE) refers to the phenomenon that the localization length of skin modes scales proportionally with system size in non-Hermitian systems. Recent studies have demonstrated that scale-free NHSE can be induced through various mechanisms, including critical NHSE, local non-Hermiticity, and boundary impurity effect. Nevertheless, these methods require careful modeling and precise parameter tuning. In contrast, our research suggests that scale-free NHSE is a universal phenomenon, observable in extensive systems as long as these systems can be described by non-Bloch band theory and host Bloch points on the energy spectrum in the thermodynamic limit. Crucially, we discover that the geometry of the GBZ determines the scaling rule of the localization length, which can scale either linearly or quadratically with the system size. Our study enriches the phenomenon of scale-free NHSE.

I. INTRODUCTION

In contrast to Hermitian operators, which guarantee real eigenvalues and conserve probability, non-Hermitian Hamiltonians provide a more general framework for the study of open or dissipative systems. This paradigm unveils previously unexplored physical phenomena that lack Hermitian analogs [1–12] and has a wide range of applications including quantum sensing [13–15], topological photonics [16–18], signal amplification [19–23], etc. The most unique phenomenon observed in non-Hermitian systems is the non-Hermitian skin effect (NHSE) [24–38], in which the eigenstates of the system are exponentially localized at the boundaries under open-boundary condition (OBC). To comprehensively account for NHSE and the corresponding energy spectrum under OBC, a complete theory, known as non-Bloch band theory [38–40], has been established.

Recent theoretical and experimental work has expanded our understanding of NHSE. A new characteristic of NHSE has been identified, wherein the localization length of skin modes scales with the system size, a phenomenon termed scale-free NHSE or scale-free localization. This effect has been observed in systems that exhibit critical NHSE [41, 42], local non-Hermiticity [43, 44], or boundary impurity effect [45]. Nevertheless, such systems require careful modeling and fine parameter tuning, manifesting remarkable alterations in the energy spectrum configuration as the system size varies.

In this work, we uncover that scale-free NHSE is a ubiquitous phenomenon, observable in extensive systems as long as these systems can be described by non-Bloch band theory and host Bloch points on the energy spectrum in the thermodynamic limit. The appearance of Bloch points stems from the intersection of the generalized Brillouin zone (GBZ) with the conventional Brillouin zone (BZ), which can be achieved by adjusting the pa-

rameters of the system. Within these usual models, the energy spectrum configuration remains largely invariant with respect to system size, thereby allowing us to elaborate the scaling rule of this type of scale-free NHSE via non-Bloch band theory. To emphasize the universality of scale-free NHSE, we derive formulas that accurately describe the power-law behaviors near the Bloch point and verify the applicability of these formulas in more complicated models. Crucially, based on these formulas, we demonstrate that different geometries of GBZ yield scale-free power-law behaviors of inverse localization length κ_m with increasing system size L : $\kappa_m \sim L^{-j}$ with distinctive exponents j that can be not only 1 but also 2. Our study provides new insights into the physical mechanisms behind the scale-free NHSE.

II. GBZ AND BLOCH POINT

Without loss of generality, we begin with a single-band tight-binding non-Hermitian model in one dimension with Bloch Hamiltonian:

$$H(k) = t_{-2}e^{-2ik} + t_{-1}e^{-ik} + t_1e^{ik}, \quad (1)$$

where k denotes the Bloch wave number that reside in the BZ, with $k \in [-\pi, \pi]$. For simplicity, the hopping parameters t_{-2} , t_{-1} , and t_1 are set to be real. The Bloch Hamiltonian describes non-Hermitian systems with periodic boundary conditions (PBC), but it fails to represent non-Hermitian systems with OBC due to significant spectral differences caused by the presence of skin modes. To elucidate the nature of these non-Hermitian skin modes, the concept of the generalized Bloch phase factor $\beta \equiv e^{ik-\kappa}$ [38] has been introduced, where κ is a real number representing the inverse localization length of the skin modes. In the thermodynamic limit, the OBC spectrum E_{OBC} is determined by evaluating the generalized Bloch Hamiltonian $H(\beta)$ along a uniquely defined contour, termed the GBZ. The $H(\beta)$ corresponding to Eq. (1) is given by

$$H(\beta) = t_{-2}\beta^{-2} + t_{-1}\beta^{-1} + t_1\beta. \quad (2)$$

* Corresponding author: fuxiangli@hnu.edu.cn

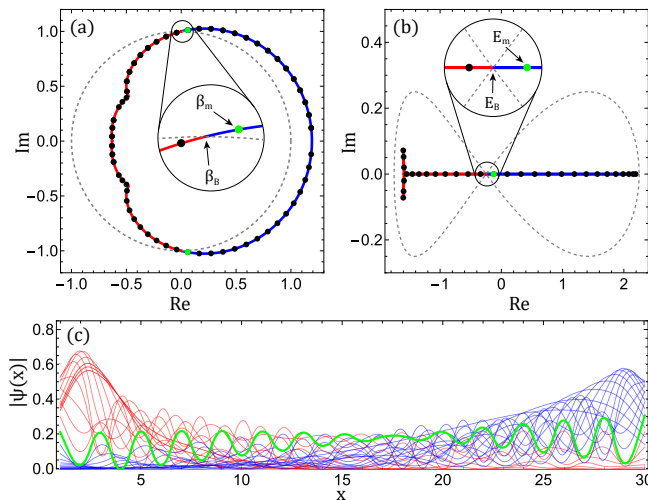


FIG. 1. (a) GBZ (solid curve) and BZ (dashed unit circle) are plotted for model Eq. (1). The part of GBZ inside (outside) BZ is colored red (blue). (b) OBC spectrum E_{OBC} (colored curve) and PBC spectrum E_{PBC} (dashed loop). The generalized Bloch phase factors and eigenenergies of the open chain with length $L = 30$ are plotted as dots in (a) and (b), where the green dots correspond to the specific energy level E_m that we are interested in. (c) Eigenfunctions corresponding to the dots on the red (blue) part of the GBZ are plotted as red (blue) curves, where the green curve corresponds to the energy level E_m . In all plots, parameters are set as $t_{-2} = 1/4$, $t_{-1} = 1$ and $t_1 = 1$.

The OBC spectrum E_{OBC} and the GBZ of $H(\beta)$ can be determined by solving the following characteristic equation

$$f(\beta, E_{\text{OBC}}) = H(\beta) - E_{\text{OBC}} = 0. \quad (3)$$

For this model, the characteristic equation yields three solutions β_j with $j = 1, 2, 3$ for a given E_{OBC} . The GBZ can be determined by setting $|\beta_2| = |\beta_3|$ after one orders the three solutions in ascending magnitude as $|\beta_1| \leq |\beta_2| \leq |\beta_3|$ (see Appendix A for detailed analysis). In Fig. 1(a) and (b) the GBZ and the OBC spectrum E_{OBC} are plotted as colored lines, whereas the BZ and the PBC spectrum E_{PBC} are plotted as dashed lines. As evident from Fig. 1(a), the GBZ intersects the BZ at two distinct points, one of which is denoted as β_B for later use. These intersection points correspond to an identical energy level, referred to as the Bloch point E_B . As elaborated in Ref. [28], E_B is the intersection of the spectra E_{PBC} and E_{OBC} , as shown in Fig. 1(b).

In addition to determining the OBC spectrum E_{OBC} , GBZ also provides valuable information about the eigenstates under OBC. Typically, GBZ is not a unit circle like BZ but has some irregular structure. The segment of GBZ that lies inside (outside) the unit circle corresponds to a set of the left (right)-localized skin modes [29, 38]. At the energy level E_B , the eigenstate extend as Bloch wave owing to $|\beta_B| = 1$ and $\kappa = 0$. Away from the Bloch point, the eigenstates are all localized either on the right or left

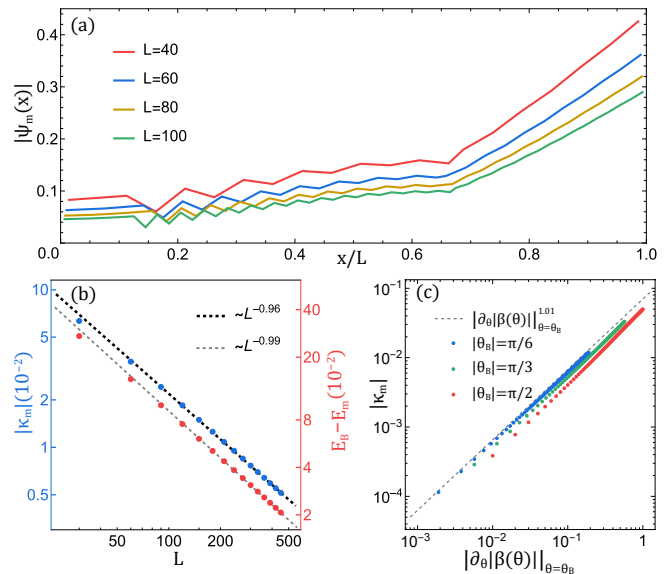


FIG. 2. (a) The rescaled profiles of the wavefunction $\Psi_m(x)$ at energy level E_m with system sizes $L = 40, 60, 80,$ and 100 (red, blue, orange, green, respectively) are displayed. The peaks of the original wavefunctions are extracted and depicted for clarity. (b) The inverse localization length κ_m (left ticks, blue) and the difference between E_m and E_B (right ticks, red) are shown to decrease as $\sim L^{-1}$. Parameters are $t_{-2} = t_{-1} = t_1 = 1$ for both (a) and (b). (c) The dependence of $|\kappa_m|$ on $|\partial_\theta |\beta(\theta)| |_{\theta=\theta_B}$ is plotted. The red, green, and blue dots correspond to three cases where $|\theta_B| = \pi/2, \pi/3,$ and $\pi/6$, respectively, and the system size is $L = 40$.

end of the system under OBC. In the model Eq. (2) for a system of size $L = 30$, the generalized Bloch phase factors β and eigenenergies E are denoted by discrete dots in Figs. 1(a) and (b), respectively. Moreover, the normalized wavefunctions are plotted in Fig. 1(c), where the left (right)-localized eigenstates are colored red (blue).

III. SCALE-FREE NHSE IN SINGLE-BAND SYSTEMS

A. Scale-free NHSE near Bloch Point

We proceed to investigate the occurrence of the scale-free NHSE near Bloch point. After arranging the energy levels based on the real parts of the eigenenergies, we focus our attention on the lowest energy level above the Bloch point, labeled E_m , for subsequent analysis. (Later we will show that the other energy levels nearest to the Bloch point in the complex plane also exhibit scale-free NHSE.) In Fig 1, the energy level E_m , its associated generalized Bloch phase factor β_m , and the magnitude of the wavefunction $\Psi_m(x)$ at E_m are highlighted in green. Notably, β_m is situated near the intersection between the GBZ and the conventional BZ, which leads to κ_m being approximately 0, and as a result, the wavefunction $\Psi_m(x)$

is less localized in comparison to the other wavefunctions.

Throughout our investigation, we calculated eigenstate at the energy level E_m for various system sizes. Remarkably, these eigenstates maintain similar configurations if the system size is taken as the measure of length, as illustrated in Fig. 2(a). This suggests that, unlike usual exponentially decaying wavefunctions with fixed localization length, the localization length of the wavefunction at the energy level E_m is proportional to the system size, a salient characteristic of the scale-free NHSE. It should be noted that variations in the amplitude of the wavefunctions across different system sizes are a consequence of wavefunction normalization. To further elucidate the scale-free power-law behavior, we calculate the inverse localization length κ_m at energy level E_m for different system sizes. As shown by the blue dots in Fig. 2(b), the inverse localization length κ_m is inversely proportional to the system size L , i.e. $\kappa_m \sim L^{-1}$. Such unique scale-free eigenmode arises due to the convergence of E_m and E_B as the system size L increases [41, 42]. Specifically, $|E_B - E_m| \sim L^{-1}$, as denoted by the red dots in Fig. 2(b).

B. Influence of the geometry of GBZ

As demonstrated in Ref. [46], the presence of cusps on the GBZ gives rise to non-Bloch van Hove singularities, thereby affecting the asymptotic behavior in the vicinity of the cusps. Given this, we conjecture that the geometry of GBZ may also affect the power-law relation near Bloch point. Our study is then extended to investigate the influence of the GBZ geometry on the scale-free NHSE. For this purpose, we first introduce $\beta_B = e^{i\theta_B}$ at Bloch point, and rewrite Eq. (2) as

$$H(\theta_B) = t_{-2}e^{-2i\theta_B} + t_{-1}e^{-i\theta_B} + t_1e^{i\theta_B} = E_B. \quad (4)$$

To simplify, we judiciously choose parameters to ensure that E_B resides on the real axis. Under these conditions, we obtain the following expressions for θ_B and E_B :

$$\theta_B = \pm \arccos \frac{t_1 - t_{-1}}{2t_{-2}}, \quad E_B = \frac{t_1^2 - t_{-2}^2 - t_1 t_{-1}}{t_{-2}}, \quad (5)$$

where we assume $\theta_B \in [-\pi/2, \pi/2]$. After parameterizing the GBZ as $\beta = |\beta(\theta)|e^{i\theta}$, the geometry of GBZ near the Bloch point can be characterized by the magnitude of $|\partial_\theta|\beta(\theta)||_{\theta=\theta_B}$. According to Eq. (5), we can modify the shape of GBZ by varying the value of $|\partial_\theta|\beta(\theta)||_{\theta=\theta_B}$ while keeping θ_B constant. Fig. 2(c) illustrates that $|\kappa_m|$ is proportional to $|\partial_\theta|\beta(\theta)||_{\theta=\theta_B}$ when L and θ_B are kept constant. The data sets, differentiated by color, indicate that the intersection locations between GBZ and BZ exert negligible influence on $|\kappa_m|$. Thus far, we have discovered that the geometry of GBZ significantly impacts the scale-free NHSE. In Sec. III C, we will further examine this effect by analyzing three specific scenarios.

C. Special cases of the geometry of GBZ

When modifying the geometry of GBZ, three notable scenarios may arise: BZ intersects GBZ at a cusp, at a saddle point (satisfying $\partial_\beta H(\beta) = 0$ [24]), or at a higher-order saddle point that is also a cusp.

In Fig. 3(a1), the BZ passes right through the cusps of the GBZ, marked by the red crosses. These cusps correspond to discontinuous points of $\partial_\theta|\beta(\theta)||_{\theta=\theta_B}$. The GBZ is partitioned into different colored sections by these cusps, each corresponding to different branches of the OBC spectrum E_{OBC} , as illustrated in Figs. 3(a1) and (a2). Additionally, the branch point of the OBC spectrum marked by the red cross in Figure 3(a2) is also a Bloch point that corresponds to the four cusps of the GBZ. For our study, we select the energy level nearest to the Bloch point on the orange branch of the OBC spectrum and label it as $E_{m'}$. As the system size increases, the energy level $E_{m'}$ gradually approaches the Bloch point. Simultaneously, the generalized Bloch phase factor $\beta_{m'}$ at the energy level $E_{m'}$ converges towards the cusp and remains within the orange segment of the GBZ. Consequently, the discontinuity of $\partial_\theta|\beta(\theta)||_{\beta=\beta_B}$ at the cusps do not affect the scale-free NHSE. Fig. 3(a3) demonstrates the scale-free power-law behaviors of $|\kappa_{m'}|$ and $|E_B - E_{m'}|$.

In Fig. 3(b1), the GBZ and the BZ are tangent at the saddle point of the GBZ, marked by a black circle. The Bloch point in this case is located precisely at the right endpoint of the OBC spectrum [40, 46], as depicted by a black circle in Fig. 3(b2). Here we still use E_m to represent the energy level closest to the Bloch point. It is worth noting that the scale-free power law behaviors change significantly due to $|\partial_\theta|\beta(\theta)||_{\theta=\theta_B} = 0$ in this case. As illustrated in Fig. 3(b3), both $|\kappa_m|$ and $|E_B - E_m|$ decrease as $\sim L^{-2}$, which is in stark contrast to the previous cases.

In Fig. 3(c1), an special intersection emerges between the GBZ and the BZ. Although it may appear as a cusp, it is, in fact, a third-order saddle point of the GBZ, denoted by a blue diamond. The l -th order saddle point of the GBZ is defined as $H(\beta) - E_S = \partial_\beta H(\beta)|_{\beta=\beta_S} = \dots = \partial_\beta^{l-1} H(\beta)|_{\beta=\beta_S} = 0$, where β_S denotes the saddle point and E_S denotes the saddle point energy. This unique geometry of the GBZ leads to the interesting phenomenon that the scale-free power-law behaviors of $|\kappa_m|$ and $|E_B - E_m|$ with respect to system size L are no longer the same, as shown in Fig. 3(c3).

Upon analyzing these three cases, it becomes evident that the geometry of GBZ significantly impacts the scale-free power law behaviors of $|\kappa_m|$ and $|E_B - E_m|$. Intriguingly, we also observe that the scale-free power-law exponent of $|E_B - E_m|$ equals the order l of the saddle point, i.e. $|E_B - E_m| \sim L^{-l}$. This finding motivates us to formulate equations for computing these exponents.

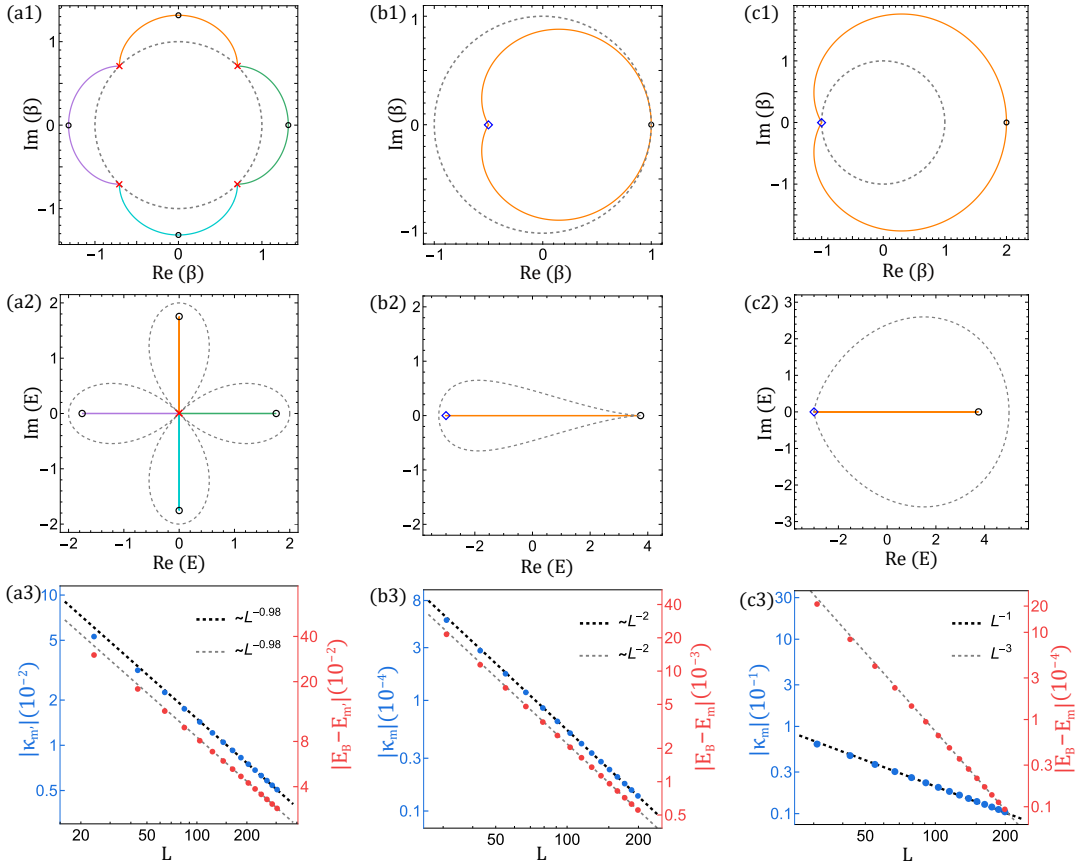


FIG. 3. GBZ and BZ, E_{OBC} and E_{PBC} , and the scale-free power-law behaviors of inverse localization length and eigenenergy near the Bloch point are plotted for $H(\beta) = \beta^{-3} + \beta^1$ in (a1)-(a3), $H(\beta) = \beta^{-2}/4 + 3\beta^{-1}/2 + 2\beta$ in (b1)-(b3), and $H(\beta) = \beta^{-2} + 3\beta^{-1} + \beta$ in (c1)-(c3). The parts of GBZ and E_{OBC} that match in color correspond to each other. (a3), (b3), and (c3) exhibit three distinct scale-free power-law behaviors.

D. Derivation of scale-free power-law exponents

In order to obtain the exponents that governing the scale-free power-law behavior near Bloch point, we now derive algebraic expressions. The density of states near bloch point can be determined as

$$\rho(E) \sim |E - E_B|^{-\alpha}. \quad (6)$$

In the parity-time (PT) symmetric phase, where E_{OBC} is purely real, the exponent α for a l -th order saddle point is $\alpha = 1 - 1/l$ [46]. Moreover, the eigenenergy E_m can be expanded near the β_B as

$$E_m \approx H(\beta_B) + \left. \frac{\partial^l H(\beta)}{\partial \beta^l} \right|_{\beta=\beta_B} (\beta_m - \beta_B)^l. \quad (7)$$

This derivation yields the relationship between the eigenenergy E_m and the inverse localization length κ_m , given by $E_m - E_B \sim (\beta_m - \beta_B)^l = e^{i\theta_B l} (e^{i(\theta_m - \theta_B)} - \kappa_m - 1)^l$, where κ_B is omitted since it is equal to 0. To further eliminate the variables θ_m and θ_B , we can express them in terms of κ_m . Employing the method utilized to define the

saddle point order on the GBZ, we can set an order j for $\kappa(\theta)$ such that $\partial_\theta \kappa(\theta)|_{\theta=\theta_B} = \dots = \partial_\theta^{j-1} \kappa(\theta)|_{\theta=\theta_B} = 0$. It should be noted that the inverse localization length $\kappa(\theta) = -\log|\beta(\theta)|$ can be obtained directly from the parametric equations of the GBZ. We then expanded κ_m around θ_B to the j -th order as $\kappa_m \approx (\theta_m - \theta_B)^j/A$, where $A = [j!/\partial_\theta^j \kappa(\theta)]_{\theta=\theta_B}$. Utilizing these expressions, we establish that $|E_m - E_B| \sim |(iA\kappa_m^{\frac{1}{j}} - \kappa_m)^l|$, where we have used the equivalent infinitesimal substitution $e^{iA\kappa_m^{\frac{1}{j}} - \kappa_m} - 1 \sim iA\kappa_m^{\frac{1}{j}} - \kappa_m$ since $\kappa_m \rightarrow 0$ when system size $L \rightarrow \infty$. We note that κ_m is of the same order or a higher-order infinitesimal compared to $\kappa_m^{\frac{1}{j}}$ since j is a positive integer. This means that the relationship between the eigenenergy E_m and the inverse localization length κ_m can be rewritten as

$$|E_m - E_B| \sim |\kappa_m|^{\frac{l}{j}}, \quad (8)$$

regardless of the value of the order j . Upon integrating both sides of Eq. (6) over the energy interval $[E_B^+, E_m^+]$ and considering that only a single energy level (i.e., E_m) falls within this interval, the system size dependence of

the energy difference $|E_m - E_B|$ can be described as:

$$|E_m - E_B| \sim L^{-l}. \quad (9)$$

Now by substituting Eq. (8) into Eq. (9), we deduce a scale-free power-law relationship between the inverse localization length κ_m and the system size L :

$$|\kappa_m| \sim L^{-j}. \quad (10)$$

Eqs. (9) and (10) accurately describe the power-law behaviors observed in Figs. 3(a3), (b3) and (c3), with the exponents l and j determined by the geometry of the GBZ. Notably, although initially derived within the PT-symmetric phase, our numerical findings affirm the applicability of these equations to the PT-symmetric broken phase as well.

IV. SCALE-FREE NHSE IN MULTIBAND SYSTEMS

Such scale-free NHSE as we found near Bloch point can also occur in multiband systems including the non-Hermitian Su-Schrieffer-Heeger model, which is pictorially shown in Fig. 4(a). The generalized Bloch Hamiltonian reads $H(\beta) = R_+(\beta)\sigma_+ + R_-(\beta)\sigma_-$, where $\sigma_{\pm} = (\sigma_x \pm i\sigma_y)/2$, and $R_{\pm}(\beta)$ are given by

$$\begin{aligned} R_+(\beta) &= t_1 + t_2\beta^{-1} + (t_3 + \gamma)\beta, \\ R_-(\beta) &= t_1 + t_2\beta + (t_3 - \gamma)\beta^{-1}. \end{aligned} \quad (11)$$

Therefore the eigenvalue equation can be written as

$$R_+(\beta) R_-(\beta) = E^2, \quad (12)$$

which is a quartic equation for β . Upon arranging the four solutions in ascending magnitude, denoted as $|\beta_1| \leq |\beta_2| \leq |\beta_3| \leq |\beta_4|$, the GBZ is determined by the trajectory of β_2 and β_3 satisfying the condition $|\beta_2| = |\beta_3|$, as shown in Figs. 4(b1) and (c1). The scale-free power-law exponents l and j assume the value of 1 [Fig. 4(b3)] when the GBZ merely intersects the BZ [Fig. 4(b1)], and 2 [Fig. 4(c3)] when the GBZ is tangent to the BZ [Fig. 4(c1)]. Interestingly, the Hamiltonian for this model manifests sublattice symmetry, $\sigma_z^{-1}H(\beta)\sigma_z = -H(\beta)$, thereby ensuring the existence of topological edge modes under specific parameter conditions [Fig. 4(b2)]. Nevertheless, the presence of zero-energy topological edge modes does not affect the scale-free NHSE, as the zero-energy modes resides within the bulk band gap. These numerical results are consistent with the theoretical predictions mentioned earlier.

V. SUMMARY

In this paper, our study focuses on a novel type of scale-free non-Hermitian skin effect (NHSE) that occurs

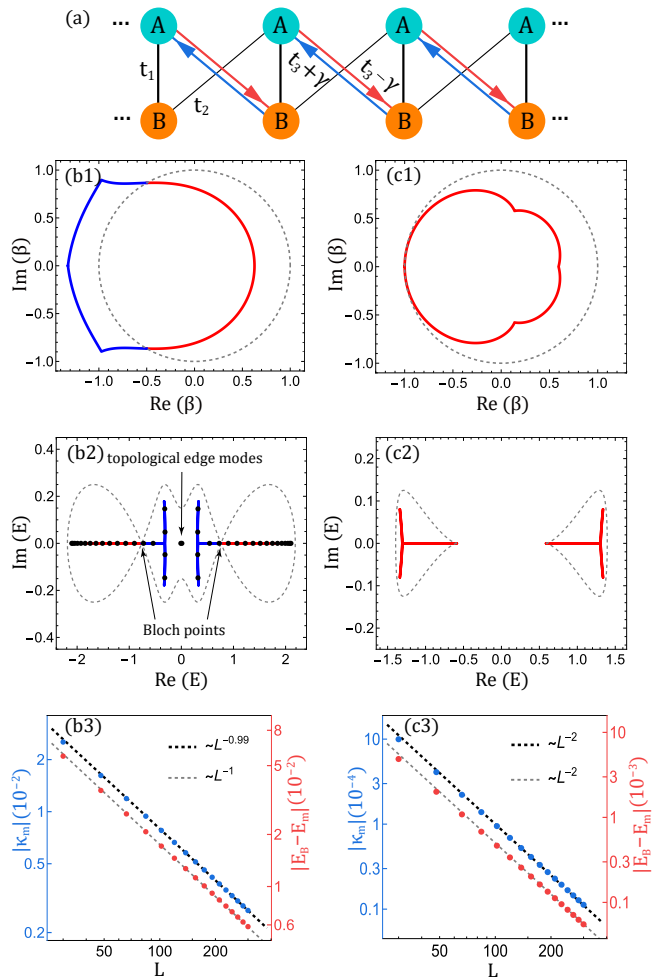


FIG. 4. (a) SSH model with alternating t_1 , t_2 hoppings and a non-Hermitian $t_3 \pm \gamma$ hopping. (b1)-(b3) are plot with parameters $t_1 = t_2 = 1$, $t_3 = 1/5$, $\gamma = 1/4$. Black dots in (b2) represent the eigenenergies of the system with $L = 20$. (c1)-(c3) are plot with parameters $t_1 = 1$, $t_2 = 1/2$, $t_3 = -1/10$, $\gamma = 1/4$. These two different scale-free power-law behaviors shown by the two-band model are consistent with those in the single-band model.

near Bloch point. We observe that the wavefunction at the energy level closest to Bloch point exhibits a scale-free property as L varies. This type of scale-free NHSE is a ubiquitous phenomenon, observable in extensive systems as long as these systems can be described by non-Bloch band theory and host Bloch points on the energy spectrum in the thermodynamic limit. Moreover, we find that the geometry of the generalized Brillouin zone affects the scale-free power-law behaviors near the Bloch point. We have derived formulas describing these scale-free power-law behaviors based on the Bloch energy band theory, thereby underscoring the universality of scale-free NHSE. In contrast to the methods used in Refs. [41–45], which require careful modeling and fine parameter tuning, our approach only necessitates rough parameter adjustments

to achieve scale-free NHSE. We expect that our theoretical predictions can be verified in various non-Hermitian platforms, including electric circuit [41, 45, 47, 48] and photonic crystals [49, 50], where NHSE has been realized.

ACKNOWLEDGEMENTS

This work was supported by the National Key Research and Development Program of the Ministry of Science and Technology (Grant No. 2021YFA1200700), the National Natural Science Foundation of China (Grant No. 11905054 and No. 12275075), and the Fundamental Research Funds for the Central Universities of China.

Appendix A: Derivation of the GBZ form Eq. (2)

In this Appendix, we briefly explain the derivation of the GBZ of the single-band model Eq. (2). In real space, the Hamiltonian of this model with the system size L reads

$$\hat{H} = \sum_{i=1}^L t_{-2} \hat{c}_{i+2}^\dagger \hat{c}_i + t_{-1} \hat{c}_{i+1}^\dagger \hat{c}_i + t_1 \hat{c}_i^\dagger \hat{c}_{i+1}, \quad (\text{A1})$$

and the real space eigenequation leads to

$$t_{-2} \psi_{n-2} + t_{-1} \psi_{n-1} + t_1 \psi_{n+1} = E_{\text{OBC}} \psi_n \quad (\text{A2})$$

in the bulk of chain, where $n = 3, 4, \dots, L-1$. The boundary condition satisfy

$$\begin{aligned} t_1 \psi_2 &= E_{\text{OBC}} \psi_1, \\ t_{-1} \psi_1 + t_1 \psi_3 &= E_{\text{OBC}} \psi_2, \\ t_{-2} \psi_{L-2} + t_{-1} \psi_{L-1} &= E_{\text{OBC}} \psi_L. \end{aligned} \quad (\text{A3})$$

Then, by substituting the general solution [38]

$$\psi_n = \sum_{j=1}^3 c_j \beta_j^n \quad (\text{A4})$$

to Eq. (A3), one can reduce the problem into the following matrix equation

$$H_B \begin{pmatrix} c_1 \\ c_2 \\ c_3 \end{pmatrix} = \begin{pmatrix} A_1 \beta_1 & A_2 \beta_2 & A_3 \beta_3 \\ B_1 \beta_1^2 & B_2 \beta_2^2 & B_3 \beta_3^2 \\ C_1 \beta_1^L & C_2 \beta_1^L & C_3 \beta_1^L \end{pmatrix} \begin{pmatrix} c_1 \\ c_2 \\ c_3 \end{pmatrix} = 0, \quad (\text{A5})$$

where

$$\begin{aligned} A_j &= t_1 \beta_j - E_{\text{OBC}}, \\ B_j &= t_{-1} / \beta_j - E_{\text{OBC}} + t_1 \beta_j, \\ C_j &= t_{-2} / \beta_j^2 t_{-1} / \beta_j - E_{\text{OBC}}. \end{aligned} \quad (\text{A6})$$

Then the condition for the Eq. (A5) to have nontrivial solutions is written as [39]

$$\det[H_B] = \sum_{i \neq j \neq k=1}^3 \epsilon_{ijk} A_i B_j C_k \beta_i \beta_j^2 \beta_k^L = 0, \quad (\text{A7})$$

where the leading term can be ordered by

$$\beta_3^L \geq \beta_2^L \geq \beta_1^L \quad (\text{A8})$$

in the thermodynamic limit, since other terms are independent of L . E_{OBC} will form a continuous band in the thermodynamic limit as long as Eq. (A7) has two leading terms (i.e., $\beta_3^L = \beta_2^L$), otherwise there only exist finite solutions of E_{OBC} . Thus, the GBZ of the model Eq. (2) in the main text is determined by $|\beta_2| = |\beta_3|$. Finally, we can solve Eq. (3) numerically and then pick the solutions that satisfy the condition $|\beta_2| = |\beta_3|$, which form the GBZ in the complex plane.

Appendix B: Periodicity of the variation of κ_m with L

In this Appendix, we elucidate the periodic behavior of κ_m with respect to changes in L . Generally, as L increases, κ_m exhibits periodic oscillations rather than following a monotonic trend. The complete periodicity of κ_m is clearly observed when L increases by 1 unit each time. Figs. 5(a2) and (b2) display that as L increases, κ_m decreases while exhibiting significant periodic fluctuations. However, the main text plots, such as Fig. 2(b), do not depict the periodic variation of κ_m with L because the interval of L was set to a specific value.

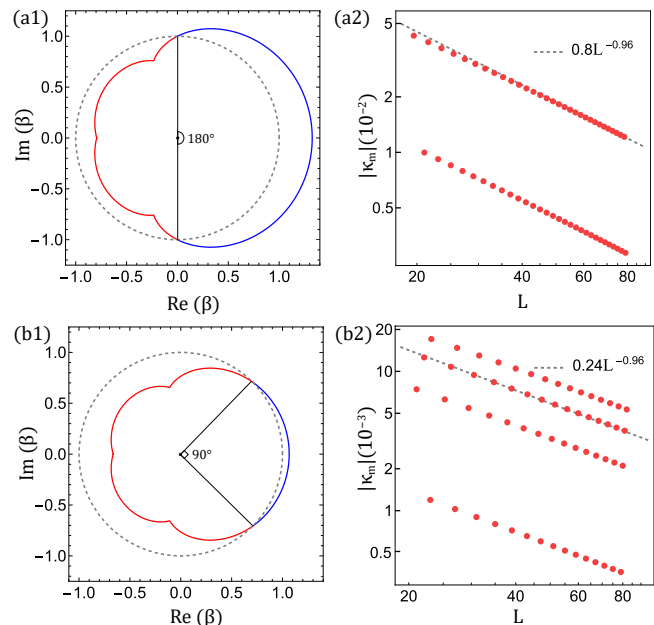


FIG. 5. GBZ and the scale-free power-law behaviors of inverse localization length near Bloch point are plotted for $H(\beta) = \beta^{-2}/2 + \beta^{-1} + \beta$ in (a1)-(a2), and $H(\beta) = \beta^{-2}/2 + \beta^{-1} + (2 + \sqrt{2})\beta/2$ in (b1)-(b2). The argument difference between the two intersections of GBZ and BZ determines the periodicity of κ_m with respect to system size L .

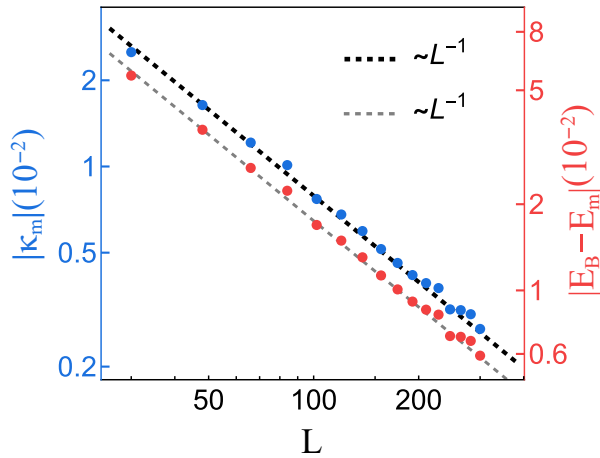


FIG. 6. Scale-free power law behaviors with weak disorders. The model is pictorially shown in Fig. 4(a), with parameters $t_1 = t_2 = 1$, $t_3 = 1/5$, $\gamma = 1/4$. However, the intracell hopping coefficients within each unit cell is randomly generated from a uniform distribution of $[t_1 - \delta t, t_1 + \delta t]$, where $\delta t = 1/100$.

Additionally, we have ascertained that the periodicity of κ_m as it varies with L is determined by the intersection points of GBZ and BZ. Specifically, the period is

calculated as $2\pi/\Delta\theta$, where $\Delta\theta$ ($\leq \pi$) represents the difference between the arguments of the two intersection points of GBZ and BZ. As shown in Fig. 5, a $\Delta\theta$ value of π ($\pi/2$) results in a period of 2 (4). There are certain special cases to consider: if 2π is not an integer multiple of $\Delta\theta$, the variation of κ_m with L may not present a clearly defined periodic pattern but still displays scale-free power-law behavior; if GBZ intersects with BZ only once, the period will be 1. Furthermore, the periodicity of $|E_B - E_m|$ as it varies with L follows a similar pattern.

Appendix C: Stability of the scale-free NHSE against disorder

In this Appendix, we examine the emergence of scale-free power-law behaviors in the presence of weak disorders. We employ the same model and parameters used in Figs. 4(b1)-(b3), with the exception that the intracell hopping coefficients within each unit cell are randomly generated from a uniform distribution $[t_1 - \delta t, t_1 + \delta t]$, where δt represents the amplitude of the disorder [51, 52]. Due to the presence of the disorder, the Bloch point and the energy spectrum in the thermodynamic limit are not accessible. Therefore, we choose the Bloch point from the clean system. In Fig. 6, it is evident that the scale-free power-law behaviors are still present even for $\delta t = 1/100$.

-
- [1] W. T. Xue, Y. M. Hu, F. Song, and Z. Wang, Non-Hermitian Edge Burst, *Phys. Rev. Lett.* **128**, 120401 (2022).
- [2] E. J. Bergholtz, J. C. Budich, and F. K. Kunst, Exceptional topology of non-Hermitian systems, *Rev. Mod. Phys.* **93**, 015005 (2021).
- [3] Y. Ashida, Z. Gong, and M. Ueda, Non-Hermitian physics, *Adv. Phys.* **69**, 249 (2020).
- [4] K. Kawabata, T. Bessho, and M. Sato, Classification of Exceptional Points and Non-Hermitian Topological Semimetals, *Phys. Rev. Lett.* **123**, 066405 (2019).
- [5] K. Zhang, Z. Yang, and C. Fang, Universal non-Hermitian skin effect in two and higher dimensions, *Nat. Commun.* **13**, 2496 (2022).
- [6] W. B. Rui, Z. Zheng, C. Wang, and Z. D. Wang, Non-Hermitian Spatial Symmetries and Their Stabilized Normal and Exceptional Topological Semimetals, *Phys. Rev. Lett.* **128**, 226401 (2022).
- [7] N. Matsumoto, K. Kawabata, Y. Ashida, S. Furukawa, and M. Ueda, Continuous Phase Transition without Gap Closing in Non-Hermitian Quantum Many-Body Systems, *Phys. Rev. Lett.* **125**, 260601 (2020).
- [8] S. Longhi, Self-Healing of Non-Hermitian Topological Skin Modes, *Phys. Rev. Lett.* **128**, 157601 (2022).
- [9] C. M. Bender and S. Boettcher, Real Spectra in Non-Hermitian Hamiltonians Having PT Symmetry, *Phys. Rev. Lett.* **80**, 5243 (1998).
- [10] C. M. Bender, M. V. Berry, and A. Mandilara, Generalized PT symmetry and real spectra, *J. Phys. A: Math. Gen.* **35** L467 (2002).
- [11] A. Mostafazadeh, Pseudo-Hermiticity versus PT symmetry: The necessary condition for the reality of the spectrum of a non-Hermitian Hamiltonian, *J. Math. Phys.* **43**, 205 (2002).
- [12] A. Mostafazadeh, Pseudo-Hermiticity versus PT - symmetry. II. A complete characterization of non-Hermitian Hamiltonians with a real spectrum, *J. Math. Phys.* **43**, 2814 (2002).
- [13] J. C. Budich and E. J. Bergholtz, Non-Hermitian Topological Sensors, *Phys. Rev. Lett.* **125**, 180403 (2020).
- [14] A. McDonald and A. A. Clerk, Exponentially-enhanced quantum sensing with non-Hermitian lattice dynamics, *Nat. Commun.* **11**, 5382 (2020).
- [15] M.a Parto, C. Leefmans, J. Williams, and A. Marandi, Enhanced sensitivity via non-Hermitian topology, *arXiv:2305.03282*.
- [16] B. Midya, H. Zhao, and L. Feng, Non-Hermitian photonics promises exceptional topology of light, *Nat. Commun.* **9**, 2674 (2018).
- [17] X. Wang, Y. Li, X. Hu, R. Gu, Y. Ao, P. Jiang, and Q. Gong, Non-Hermitian high-quality-factor topological photonic crystal cavity, *Phys. Rev. A* **105**, 023531 (2022).
- [18] E. Sliotman, W. Cherifi, L. Eek, R. Arouca, M. Bourenane, and C. Morais Smith, Topological Monomodes in non-Hermitian Systems, *arXiv:2304.05748*.
- [19] W.-T. Xue, M.-R. Li, Y.-M. Hu, F. Song, and Z. Wang, Simple formulas of directional amplification from non-Bloch band theory, *Phys. Rev. B* **103**, L241408 (2021).
- [20] L. Feng, M. Ayache, J. Huang, Y.-L. Xu, M.-H. Lu, Y.-F. Chen, Y. Fainman, and A. Scherer, Nonreciprocal Light

- Propagation in a Silicon Photonic Circuit, *Science* **333**, 729 (2011).
- [21] C. C. Wanjura, M. Brunelli, and A. Nunnenkamp, Topological framework for directional amplification in driven-dissipative cavity arrays, *Nat. Commun.* **11**, 3149 (2020).
- [22] D. Porras and S. Fernández-Lorenzo, Topological Amplification in Photonic Lattices, *Phys. Rev. Lett.* **122**, 143901 (2019).
- [23] B. Abdo, K. Sliwa, S. Shankar, M. Hatridge, L. Frunzio, R. Schoelkopf, and M. Devoret, Josephson Directional Amplifier for Quantum Measurement of Superconducting Circuits, *Phys. Rev. Lett.* **112**, 167701 (2014).
- [24] S. Longhi, Probing non-Hermitian skin effect and non-Bloch phase transitions, *Phys. Rev. Research* **1**, 023013 (2019).
- [25] L. Xiao, T. Deng, K. Wang, Z. Wang, W. Yi, and P. Xue, Observation of Non-Bloch Parity-Time Symmetry and Exceptional Points, *Phys. Rev. Lett.* **126**, 230402 (2021).
- [26] S. Weidemann, M. Kremer, S. Longhi, and A. Szameit, Topological triple phase transition in non-Hermitian Floquet quasicrystals, *Nature* **601**, 354 (2022).
- [27] N. Okuma, K. Kawabata, K. Shiozaki, and M. Sato, Topological Origin of Non-Hermitian Skin Effects, *Phys. Rev. Lett.* **124**, 086801 (2020).
- [28] F. Song, S. Yao, and Z. Wang, Non-Hermitian Topological Invariants in Real Space, *Phys. Rev. Lett.* **123**, 246801 (2019).
- [29] K. Zhang, Z. Yang, and C. Fang, Correspondence between Winding Numbers and Skin Modes in Non-Hermitian Systems, *Phys. Rev. Lett.* **125**, 126402 (2020).
- [30] S. Yao, F. Song, and Z. Wang, Non-Hermitian Chern Bands, *Phys. Rev. Lett.* **121**, 136802 (2018).
- [31] F. K. Kunst, E. Edvardsson, J. C. Budich, and E. J. Bergholtz, Biorthogonal Bulk-Boundary Correspondence in Non-Hermitian Systems, *Phys. Rev. Lett.* **121**, 026808 (2018).
- [32] C. H. Lee and R. Thomale, Anatomy of skin modes and topology in non-Hermitian systems, *Phys. Rev. B* **99**, 201103(R) (2019).
- [33] T. Helbig, T. Hofmann, S. Imhof, M. Abdelghany, T. Kiessling, L. Molenkamp, C. Lee, A. Szameit, M. Greiter, and R. Thomale, Generalized bulk-boundary correspondence in non-Hermitian topoelectrical circuits, *Nat. Phys.* **16**, 747 (2020).
- [34] L. Xiao, T. Deng, K. Wang, G. Zhu, Z. Wang, W. Yi, and P. Xue, Non-Hermitian bulk-boundary correspondence in quantum dynamics, *Nat. Phys.* **16**, 761 (2020).
- [35] A. Ghatak, M. Brandenbourger, J. van Wezel, and C. Coulais, Observation of non-hermitian topology and its bulk-edge correspondence in an active mechanical metamaterial, *Proc. Natl. Acad. Sci. U.S.A.* **117**, 29561 (2020).
- [36] S. Weidemann, M. Kremer, T. Helbig, T. Hofmann, A. Stegmaier, M. Greiter, R. Thomale, and A. Szameit, Topological funneling of light, *Science* **368**, 311 (2020).
- [37] T. E. Lee, Anomalous Edge State in a Non-Hermitian Lattice, *Phys. Rev. Lett.* **116**, 133903 (2016).
- [38] S. Yao and Z. Wang, Edge States and Topological Invariants of Non-Hermitian Systems, *Phys. Rev. Lett.* **121**, 086803 (2018).
- [39] K. Yokomizo and S. Murakami, Non-Bloch Band Theory of Non-Hermitian Systems, *Phys. Rev. Lett.* **123**, 066404 (2019).
- [40] Z. Yang, K. Zhang, C. Fang, and J. Hu, Non-Hermitian Bulk-Boundary Correspondence and Auxiliary Generalized Brillouin Zone Theory, *Phys. Rev. Lett.* **125**, 226402 (2020).
- [41] L. Li, C. H. Lee, S. Mu, and J. Gong, Critical non-Hermitian skin effect, *Nat. Commun.* **11**, 5491 (2020).
- [42] K. Yokomizo and S. Murakami, Scaling rule for the critical non-Hermitian skin effect, *Phys. Rev. B* **104**, 165117 (2021).
- [43] B. Li, H. Wang, F. Song, and Z. Wang, Scale-free localization and PT symmetry breaking from local non-Hermiticity, *Phys. Rev. B* **108**, L161409 (2019).
- [44] C. Guo, X. Wang, H. Hu, and S. Chen, Accumulation of scale-free localized states induced by local non-Hermiticity, *Phys. Rev. B* **107**, 134121 (2023).
- [45] L. Li, C. H. Lee, S. Mu, and J. Gong, Impurity induced scale-free localization, *Commun. Phys.* **4**, 42 (2021).
- [46] Y. Hu, H. Wang, Z. Wang, and F. Song, Geometric Origin of Non-Bloch PT Symmetry Breaking, [arXiv:2210.13491](https://arxiv.org/abs/2210.13491).
- [47] T. Helbig, T. Hofmann, S. Imhof, M. Abdelghany, T. Kiessling, L. Molenkamp, C. Lee, A. Szameit, M. Greiter, and R. Thomale, Generalized bulk-boundary correspondence in non-Hermitian topoelectrical circuits, *Nat. Phys.* **16**, 747 (2020).
- [48] T. Helbig, T. Hofmann, C. H. Lee, R. Thomale, S. Imhof, L. W. Molenkamp, and T. Kiessling, Band structure engineering and reconstruction in electric circuit networks, *Phys. Rev. B* **99**, 161114(R) (2019).
- [49] Q. Zhou, J. Wu, Z. Pu, J. Lu, X. Huang, W. Deng, M. Ke and Z. Liu, Observation of geometry-dependent skin effect in non-Hermitian phononic crystals with exceptional points, *Nat. Commun.* **14**, 4569 (2023).
- [50] A. Ghatak, M. Brandenbourger, J. van Wezel, and C. Coulais, Observation of non-Hermitian topology and its bulk-edge correspondence in an active mechanical metamaterial, *Proc. Natl Acad. Sci. USA* **117**, 29561 (2020).
- [51] X. Luo and C. Zhang, Photonic topological insulators induced by non-Hermitian disorders in a coupled-cavity array, [arXiv:1912.10652](https://arxiv.org/abs/1912.10652).
- [52] Z. Sun, M. Deng, and F. Li, Kibble-Zurek behavior in one-dimensional disordered topological insulators, *Phys. Rev. B* **106**, 134203 (2022).